Magnetic Resonance Imaging and Velocity Mapping in Chemical Engineering Applications

Lynn F. Gladden* and Andrew J. Sederman

University of Cambridge
Department of Chemical Engineering and Biotechnology
Pembroke Street
Cambridge CB2 3RA
U.K.

Submitted: 14 June 2016

Address for correspondence:
University of Cambridge
Department of Chemical Engineering and Biotechnology
Pembroke Street
Cambridge
CB2 3RA, UK

Lynn F. Gladden
Email: lfg1@cam.ac.uk

Andrew J. Sederman
Email: ajs40@cam.ac.uk

ARTICLE TABLE OF CONTENTS

ABSTRACT

INTRODUCTION

Underlying Principles of MRI and MR Measurements of Transport

Speeding up MR Data Acquisitions

RHEOLOGY AND PIPE FLOWS

Rheology

Pipe flows

IMAGING HYDRODYNAMICS IN REACTORS

Fixed Beds

Gas-Solid Fluidised Beds

CONCLUSIONS AND FUTURE OUTLOOK

REFERENCES

ABSTRACT

This review aims to illustrate the diversity of measurements that can be made using magnetic resonance techniques and which have the potential to provide insights to chemical engineering systems that cannot readily be achieved using any other method. Perhaps the most notable advantage in using magnetic resonance methods is that both chemistry and transport can be followed in three dimensions, in optically opaque systems and without the need for tracers to be introduced into the system. Here we focus on hydrodynamics and, in particular, applications to rheology, pipe flow, and fixed-bed and gas-solid fluidised bed reactors. With increasing development of industrially-relevant sample environments and undersampling data acquisition strategies which can reduce acquisition times to <1 s, magnetic resonance is finding increasing application in chemical engineering research.

KEYWORDS

magnetic resonance, hydrodynamics, rheology, chemical reactors, pipe flow

INTRODUCTION

From a chemical engineering perspective, the main advantage of magnetic resonance (MR) over almost any other measurement technique is that it provides information on chemical composition and transport processes non-invasively and without need for tracer particles or isotopic substitution. The measurement can be made specific to a particular molecular species or to identify the different components in a multi-component mixture. In its purest form MR methods do not rely on any model assumption to reconstruct image data; images are produced by Fourier transformation of the acquired data. Most importantly, the MR signal is directly proportional to the number of nuclear spins present; it is the quantitative nature of the MR measurement that makes it so valuable when acquiring data which can then be used to test theory or validate numerical simulation codes. This review will focus on the application of spatially-resolved magnetic resonance techniques, usually referred to as MR imaging (or MRI) and MR velocity imaging (or MR velocimetry), in the areas of rheology, pipe flows and reactor hydrodynamics, and use these to illustrate the diversity of information that MR can provide.

Underlying Principles of MRI and MR Measurements of Transport (1,2)

The intrinsic chemical-selectivity of the MR measurement arises because when a nucleus of non-zero nuclear spin quantum number is placed in an external magnetic field, B_0, its nuclear spin energy levels become non-degenerate. This energy level splitting is sensitive not only to the nucleus being studied (e.g. ^{1}H, ^{19}F) but also the chemical environment of that nucleus. By applying a radio-frequency (r.f.) pulse, a resonant absorption occurs between these nuclear spin energy levels. The specific frequency at which this resonance occurs is called the resonance (or Larmor) frequency, ω_0; which is proportional to the strength of the external magnetic field, B_0, used in the experiment and corresponds to the precession frequency with which the resonant spins rotate around $\mathbf{B_0}$:

$$\omega_0 = \gamma B_0 \tag{1}$$

where γ is the gyromagnetic ratio of the nucleus being studied. Following the r.f. excitation, the return of the nuclear spin system to thermal equilibrium is characterised by various so-called nuclear spin relaxation times; the most important of these relaxation times are the spin-lattice, T_1, and spin-spin, T_2, relaxation times. These relaxations times are not only central to being able to implement quantitative measurements but also enable characterisation of molecular-surface interaction strength which is exploited in measurements of competitive

adsorption processes in catalysis and rock core wettability (3-6) and differentiation of crystallisation and uncrystallised material (7).

The acquisition of images and transport measurements both rely on the introduction of spatially-varying magnetic fields, or gradients, in addition to the large static magnetic field B_0. The effect of introducing the spatially-varying field is that the total magnetic field now also varies with position, and hence so will the resonance frequency of the nuclear spins:

$$\omega(\mathbf{r}) = \gamma(B_0 + \mathbf{G} \cdot \mathbf{r}) \tag{2}$$

where $\mathbf{r}$ is the position vector and $\mathbf{G}$ is a vector describing the strength and direction of the applied gradient in the magnetic field. In the context of imaging, Eqn (2) leads to the Fourier pair:

$$S(\mathbf{k}) = \iiint \rho(\mathbf{r}) \exp[\mathrm{i}2\pi\mathbf{k} \cdot \mathbf{r}] \; d\mathbf{r} \tag{3}$$

$$\rho(\mathbf{r}) = \iiint S(\mathbf{k}) \exp[-\mathrm{i}2\pi\mathbf{k} \cdot \mathbf{r}] \; d\mathbf{k} \tag{4}$$

where $S(\mathbf{k})$ is the acquired signal and $\rho(\mathbf{r})$ is the spin density as a function of position; these equations have been simplified by making the substitution $\mathbf{k} = \left(\frac{\gamma \mathbf{G} t}{2\pi}\right)$, after Mansfield and Grannell (8) who introduced the concept of **k**-space upon which the development of all imaging pulse sequences is based. It follows that if we acquire data that samples all of the required **k**-space raster, $S(\mathbf{k})$, followed by Fourier transformation of these acquired data, we will recover $\rho(\mathbf{r})$, the spin density as a function of position, i.e. the image.

When acquiring image data, a nucleus of high natural abundance and high sensitivity is 'observed', such as ^{1}H. This means that any molecule containing a hydrogen atom can, in principle, be studied. Other particularly favourable nuclei for imaging are fluorine (^{19}F), sodium (^{23}Na) and phosphorus (^{31}P); this makes MR especially useful for studying, for example, pharmaceutically active species even when these exist in much lower volume fraction than their surrounding polymer or oxide matrix (9). ^{13}C imaging which is particularly useful in probing hydrocarbon conversions can be achieved whether through isotopic enrichment of the feed (which is expensive) or by 'boosting' the ^{13}C signal intensity by transfer of 'polarisation' from the adjacent ^{1}H species to the ^{13}C nucleus. The latter has been used to enable tracking of conversion in a fixed-bed reactor has (10,11). In

imaging gas flow fields in non-reacting systems, SF_6 is often used as the gas because of its high sensitivity and favourable relaxation times (12).

The use of spatial variations, or gradients, in the magnetic field to encode for position is exploited again in measurements of transport. However, instead of applying single magnetic field gradient pulses in the MR experiment (known as a 'pulse sequence'), the gradients are typically applied in pairs of short pulses (typically 1-5 ms). The action of each pulsed magnetic field gradient is to label the position of the spins along the direction of the applied gradient, with a change in the phase of their precession around $\mathbf{B_0}$. Following from Eqn (2), the rate of change of phase upon application of a pulsed gradient, **G,** is given, in the frame of reference of the spin system (i.e. removing the term due to B_0), by:

$$\frac{d\phi}{dt} = \omega(\mathbf{r}) = \gamma \mathbf{G} \cdot \mathbf{r} \,. \qquad (5)$$

The phase offset, ϕ, accrued after a short pulse of time duration δ will depend on the magnitude of the magnetic field gradient (let us assume it is applied in the z-direction) G_z, and the position, z, and is given by:

$$\phi = \int_0^{\delta} \gamma G_z z \, dt \; = \gamma G_z z \delta. \qquad (6)$$

In the simplest form of transport measurement, consider the application of a pair of pulsed gradients both of magnitude G but applied in opposite directions separated by a time interval (the observation time), Δ. If the nuclear spins (i.e. molecules) do not move along z during the observation time then the phase offsets introduced by the two equal and opposite gradients will have a net value of zero and the signal acquired at the beginning of the pulse sequence will equal that acquired at the end. However, any net translation during the time Δ will cause the signal to accrue a phase shift at the end of the pulse sequence where this phase shift is proportional to the distance moved in the z direction. Measurement of this phase shift leads to the quantitative measurement of coherent motion. If instead we consider incoherent diffusive motion, the range of displacements will lead to a range of phase shifts which, in turn, will lead to a loss of signal. This measurement of phase shift and signal attenuation, along with values of the experimental parameters, yields measurements of coherent motion (flow) and diffusion and dispersion (incoherent flow). Measurements of molecular diffusion coefficients $>10^{-14}$ m^2 s^{-1} are standard, as are measurements of flow velocities ranging from μm s^{-1} to m s^{-1} (13). For example, MR velocity imaging has been used to measure the velocities associated with both cytoplasmic streaming in

single plant cells (14) and maps of velocity vectors in the transition to turbulence (15) and at Re > 10^5 (12). Figure 1 shows the result of combining an imaging pulse sequence with a flow measurement to give a velocity map. In this example the map of water flowing through a packing of non-porous spheres is shown (16). Another type of experiment commonly used when the goal is to characterise transport phenomena is the propagator measurement; this is widely used in petrophysics to characterise transport in porous media (17-19). The propagator is the probability density function of displacement after a fixed time and gives a statistical description of the evolution of displacement characterizing the system. It is equivalent to a tracer measurement in which the tracer is introduced into the flow and the average distribution of tracer from its initial location is determined in a completely non-invasive manner. Examples of propagators acquired over different observation times for flow through two different rock core plugs are shown in Figure 2.

Speeding up MR Data Acquisitions

Figure 3 illustrates the different strategies for MR imaging data acquisitions. In each of Fig. 3 (a)-(d), the green dots identify points of the **k**-space raster, $S(\boldsymbol{k})$, which are sampled to provide the final image. In the most commonly implemented MR imaging experiments the full **k**-space raster is sampled fulfilling standard Fourier sampling requirements. In the most basic and most directly quantitative imaging experiment known as the spin warp pulse sequence (21), a single r.f. excitation of the system is followed by acquisition of a single horizontal line of **k**-space points. A second r.f. excitation, after a recovery time of order T_1, is then used to acquire data from the second line of **k**-space, and so on until the full raster is sampled; this is shown in Fig. 3a. Implementing pulse sequences which can acquire data faster has been central in enabling MR to characterize dynamic systems which has significantly widened applications in chemical engineering research.

The speeding-up of data acquisition rates takes two approaches:

(i) *Faster Sampling* involving novel gradient (sampling) trajectories through **k**-space: Fast sampling methods have been used in engineering since the early 2000s. Two approaches exist: (i) use of one r.f. excitation to sample *multiple* lines of **k**-space points; methods include Rapid Acquisition with Relaxation Enhancement (RARE) (22) and Echo Planar Imaging (EPI) (23), and (ii) rapid multiple r.f. excitations; the most common method of this type is known as Fast Low Angle Shot (FLASH) imaging (24).

Using these approaches image acquisition times can be reduced from timescales of tens of minutes down to seconds or even less (25). A sampling strategy which speeds acquisition up even further is 'spiral' imaging (26); the gradient trajectory is shown in Fig. 3b. In the spiral sequence the rate of change of strength (slew rate) made to the imaging gradients is typically significantly smaller than is used in ultra-fast rectilinear sampling strategies, with the result that the complete **k**-space raster can be sampled more quickly. Implementation of a spiral sampling strategy can reduce image acquisition times by a factor of ~4 compared to conventional rectilinear sampling of the same system. This method is also more robust to fluid flow than rectilinear sampling techniques making it more suitable for engineering applications (27).

(ii) *Undersampling* methods in which fewer **k**-space data points are acquired than are required from consideration of traditional 'sampling theory' (28,29): These concepts are certainly not restricted to MR and are long-established in, for example, radio astronomy (30,31). In MR, for a given pulse sequence, we can consider the data acquisition time to correlate with the number of data points acquired. Thus undersampling strategies can substantially reduce data acquisition times. Two such methods that are now becoming more widely used in MR are compressed sensing (CS) (32-34) and Bayesian analysis (35-38). These two approaches are illustrated in Figs. 3c and 3d, respectively.

Compressed sensing methods allow us to 'undersample' the **k**-space raster and yet still recover the original image. Care needs to be taken when implementing CS MRI measurements in application to a particular system. The best result may require optimisation of both the data sampling strategy (i.e. which **k**-space data points are sampled and in what order) and the data regularisation method adopted (39). CS MRI enables image acquisitions of dynamics systems which could not be studied using traditional full-raster sampling.

In Bayesian analysis the state of a system, θ, is inferred from a set of observations, $\hat{y}$, from the posterior probability density function $p(\theta|\hat{y})$:

$$p(\theta|\hat{y}) \propto p(\hat{y}|\theta)p(\theta) \qquad (7)$$

where $p(\hat{y}|\theta)$ is the likelihood function and $p(\theta)$ incorporates any prior knowledge of the system. In the context of speeding up data acquisition Bayesian approaches might be considered as the limiting case of undersampling. In this case the concept of an image is dispensed with. Instead, a question is posed to which an answer is given based on the data acquired, with a statistical error associated with that answer. An example of using this approach to characterise the bubble-size distribution of a two-phase gas-liquid bubbly flows is discussed later (40). The experiment takes the form of acquiring individual data points in **k**-space and performing a statistical test to see if those data points are consistent with bubbles of a given diameter or distribution of diameters. Using this approach instead of acquiring image data on a **k**-space raster which may be of size 256 × 256, only ~10 points may be needed to characterise the distribution.

RHEOLOGY AND PIPE FLOWS

MR imaging of flow is used to gain insight to fluid rheology as well as to spatially-resolve flow velocities in simple and complex pipe geometries. In application to rheology, MR is often termed Rheo-NMR and this is addressed as a separate section below. The advantage of MR in studying rheology and pipe flows is that it discriminates chemical species and phases within the flow, as well as being able to probe optically opaque systems and those with multiple phase boundaries which scatter light, thereby making many optical/laser methods inappropriate for use.

Rheology

The term Rheo-NMR is, to some extent misleading, since the technique does not currently measure stress-strain data typical of laboratory rheological characterisation simultaneously with the MR data acquisition. However, Rheo-NMR measurements do identify ‘slip’, as well as providing measurements of meso- and macro-scale structural and velocity variations in the fluid under examination which help us to understand and interpret conventional rheological measurements (41). Rheo-NMR is now widely used to characterise and understand the behaviour of complex fluids and related materials of interest in home and personal care, foods and petrophysics (42-44). Typically, MR measurements are made in cone and plate, parallel plate and Couette geometry cells identical to those used in conventional laboratory rheological measurements. Figure 4 shows the

now ‘classic’ MR image of shear banding occurring in a wormlike micelle system within a cone and plate geometry (45,46).

A more experimentally demanding Rheo-NMR measurement combines the velocity measurement with *in situ* NMR spectroscopy to investigate molecular ordering and to simultaneously compare such ordering with local strain rates during, for example, shear banding. In most cases deuterium (^{2}H) NMR spectroscopy is employed, hence requiring deuteration of the fluid of interest. The use of deuterium labelling in this system is important because the ^{2}H nucleus is quadrupolar (nuclear spin quantum number, I>½); such nuclei have spectral lineshapes which are particularly sensitive to motion, and hence can be used as fingerprint of molecular dynamics and orientation (41). Elegant demonstrations of the combined use of MR velocity imaging and ^{2}H spectroscopy, include the investigation of flow and alignment properties of wormlike micelles as a function of temperature and applied shear rate (47), and of anomalous shear banding with sufficient spatiotemporal resolution to resolve fluctuations in the flow structure along the vorticity axis and instability of the high shear band (48).

From the mid-2000s, a number of approaches to speeding up data acquisitions to study dynamic systems have been reported. For example, Brown and Callaghan (49) used rapid 2D RARE MR velocity images, with acquisition time of 3 s, and ^{2}H spectroscopy to investigate the spatio-temporal flow dynamics and, in particular, the onset of shear banding in a wormlike micelle system in a cylindrical Couette device. RARE MR velocity measurements have also been used to study the time-dependent velocity field on startup of a fluid-filled cylinder and hence measure the diffusion of vorticity (50). Another example of a time-dependent measurement (51), used a variant of the EPI technique to record the temporal evolution of the velocity field following a step change in rotation rate in a wide-gap Couette cell geometry.

Rheological characterisation using MR is not limited to the more traditional Couette, cone and plate and parallel plate measurements configurations. For example, Seymour and co-workers (52) used triggered MR velocity imaging to study a range of Newtonian and non-Newtonian fluids under conditions of oscillatory flow. The concept of triggering is now routinely used in both medical and non-medical MR, and it enables signal averaging in data acquisition in periodically varying systems. The spectrometer is triggered to acquire data at the same point in each cycle thereby avoiding temporal blurring. A quite different example, is that of Blythe *et al*. (53) who proposed a method to enable rheological characterisation *in situ* during pipe flow. The approach

used is based on the acquisition of MR propagators but there are two novel aspects of the implementation which make the process application possible. First, the raw data are analysed (i.e., no Fourier transformation to the propagator is performed); and second, undersampling is employed such that the number of data points acquired is reduced by a factor of 32 relative to a fully-sampled acquisition. This approach enables data acquisition times 3% of those than would be required using traditional MR measurements.

The applications of MR to emulsion characterisation extends beyond rheological characterisation of the fluid (42). MR also provides an elegant, non-invasive method of measuring the emulsion droplet size distribution in macroemulsions. Emulsion droplet sizing using MR employs pulsed field gradient measurements of molecular diffusion and 'tunes' the measurement to the chemical species comprising the droplet phase. The principle of the measurement is that the root-mean-square (rms) displacement of the molecules contained within the droplet is measured, usually as a function of increasing observation time; the rms and therefore signal attenuation increases as observation time increases and then becomes constant as the rms displacement approaches that of the droplet dimension. Packer and Rees (54) were the first to demonstrate this technique and it is now widely used. The MR method of droplet sizing is particularly useful because it is both non-invasive and *in situ*; in this regard it has clear advantages over measurements in which a sample of the emulsion has to be extracted from the process line and introduced to a new measurement environment. Further, it can equally easily be applied to systems such as concentrated emulsions, freezing emulsions, multiple emulsions and suspo-emulsions; many of which cannot be studied using light scattering techniques (55). Droplet-size characterisation of emulsions is a measurement which has now been demonstrated on low magnetic field hardware; in particular, a 1.1 T bench-top NMR magnet (56), which is the type of low-cost hardware that could be used in a process application.

Rheological characterisation of particular suspensions (including high solids fractions approaching what are thought of as granular systems) is an area of increasing interest. Examples include studies of model yield stress fluids of relevance to the characterisation of mortars and concretes (57). At a more fundamental level, conventional rheometry and spatially-resolved MR measurements of solids concentration across the gap of a Couette cell have been used to follow the emergence of discontinuous shear thickening in cornstarch (58); the flow of dry and wet granular media in a Couette geometry to test the applicability of the "fluidity model" for nonlocality in these materials (59); pressure-driven suspension flow near jamming (60); and the stability of colloidal gels (61).

Pipe Flows

In most studies of pipe flows reported to date, in-plane spatial resolutions of 100-400 μm are typical within pipes of several cm in diameter; 6 cm is the largest diameter pipe that can be used inside standard commercial superconducting magnets. However, by reducing the field-of-view, which is defined by the diameter of the receiver coil, spatial resolution of ~20 μm can be achieved which enable flow fields in microchannels to be imaged. MR can be directly applied to channels of any cross-section. Examples include tracking mixing and flow velocity downstream of a Y-junction microchannel with a spatial resolution of 23 μm × 23 μm, obtained for a channel of rectangular cross section 250 μm × 250 μm (62), and chemically-resolved imaging with a spatial resolution of 32 μm × 32 μm within a channel of circular cross-section of internal radius 400 μm (63).

Expansion during pipe flow provides a number of examples of how MR can be used. Xia et al. (64) first used MR velocimetry to image velocity profiles and instabilities downstream of an abrupt expansion as Reynolds number (Re) was increased. The inlet pipe was 8 mm in diameter and 1.23 m in length. Radial profiles with a spatial resolution of 20 μm were acquired across the channel diameters. A more recent example employs a bespoke MR pulse sequence implementation to identify asymmetries in the flow that develop downstream of an expansion (65). The inlet pipe was 8 mm in diameter, with a sudden expansion into a second pipe of 16 mm diameter. To do this an MR technique was developed which identified only the spatial location of stagnant (and near-stagnant molecules) across the pipe. Figure 5 shows examples of the type of data that were obtained; these data provided evidence for a steady symmetry breaking bifurcation at a critical value of Re.

The use of MR to study flow though expansions or contractions is, of course, equally applicable to multi-phase systems. The added value of using MR in these applications is that we can, in principle, often obtain spatially-resolved maps of the distribution of each phase and their velocity. Early work in studying the effect of flow through an expansion includes: the structuring of gelled suspensions as a result of flowing through a sudden expansion (66), and the effect of inlet conditions on the neutrally-buoyant solids distribution and velocity fields in concentrated

suspension flows (67). More recently, McCarthy and Powell and co-workers recorded MR velocity profiles of cellulosic suspensions flowing in a horizontal pipe and reported how the flow profiles changed as a function of fibre concentration, flow rate and fibre type (68). Recognition of MR as a technique for flow metering has long been recognised (69), and is currently of particular interest to the oil and gas sector engaging both academic and industrial research laboratories (70,71), as evidenced by an increasing patent literature in this space. Whilst the principles are well-established it is the advent of easy-to-use low-field MR hardware and the increased confidence in using under-sampling methods that have generated renewed activity on this space.

Gas-liquid bubbly flows provide an example of a multi-phase system in which a wealth of different types of MR experiment have been applied. Two methods have recently been reported to determine gas bubble-size distributions in gas-liquid bubbly flows; these form an excellent example of undersampling approaches (see Fig. 3). The experiments were performed in a vertical column of internal diameter 31 mm and at gas voidages up to ~40%. The first used ultra-fast spiral imaging to acquire 2D images in the transverse direction at a rate of 55 frames per second and a spatial resolution of 578 μm × 578 μm (72). From these data, bubble size distribution, and bubble shape and interfacial area were calculated. The second approach (73) exploits the Bayesian undersampling approach, having recognised that if it is the bubble-size *distribution* that is required we do not actually need all the information that is contained in an image; we are only interested in the dimension of the bubbles. Given that a bubble of a specific dimension will have a unique 'fingerprint' in **k**-space; it is possible to extract the bubble-size distribution consistent with the acquired **k**-space data. The main assumption made in the analysis is the bubble shape. Bubble-size distribution measurements were recorded every 3.2 s thereby enabling time-resolved measurements. To demonstrate this, a surfactant stream was injected into the air-water flow and the change in bubble shape as well as the bubble-size distribution tracked as the surfactant stream was switched on and then off.

On a somewhat more academic note undersampled, ultra-fast spiral acquisition combined with compressed sensing reconstructions have been used to image the liquid velocity field around a rising bubble (74). By recording velocity images at a rate of 63 frames per second it was possible to observe the flow field around the rising bubble; potential flow about the nose of the bubble and periodic vortex shedding in the bubble wake are seen (Figure 6). Further, by recording 2D velocity maps in the transverse plane as well, it was possible to gain insight into why a bubble changes

direction (i.e., ‘wobbles’) as it rises through a column of water; this is a good example of new MR measurements giving insight to long-standing questions in fluid mechanics (75,76).

IMAGING HYDRODYNAMICS IN REACTORS

To date, the majority of MR studies applied to chemical reactors have focussed on imaging flow fields; gas, liquid and solids flow fields have been imaged (77,78). The majority of studies have focussed on fixed bed and gas-solid fluidised bed systems, although single-phase gas and gas-liquid flow in ceramic monoliths have been reported (79-84). The ability to map chemical conversion within a working reactor is possible and studies have focused on reactions occurring in fixed beds. Early experiments include the spatial mapping of the esterification of methanol and acetic acid over a bed of acidic ion exchange resin (85), and the tracking of conversion along a fixed bed during the hydrogenation of α-methylsytrene over a fixed bed of Pd/Al_2O_3 catalyst (86) and associated liquid distribution effects (87). To achieve discrimination between reactants, intermediates and products, it is advantageous, and sometimes essential, to exploit the large spectral frequency range associated with ^{13}C observation compared to ^{1}H observation. Extension of MRI spatial mapping of conversion using ^{13}C MRI has been demonstrated in application to the competitive etherification and hydration reactions of 2-methyl-2-butene within a fixed bed of ion exchange resin (10), and then applied to the spatial mapping of alkene isomerisation and hydrogenation during the hydrogenation of 1-octene occurring in a fixed-bed of Pd/Al_2O_3 catalyst (11). The use of *in situ* temperature measurement by spectroscopic analysis of ethylene glycol contained with small bulbs placed within the reactor has also been demonstrated with respect to 1-octene hydrogenation (88) and ethene hydrogenation (89).

The implementation of spatially-resolved mapping of conversion within reactors has lagged relative to imaging of hydrodynamics for two main reasons; in both, advances are currently being made. First, reactors that operate at industrially-relevant conditions and are compatible with operation inside a large superconducting magnetic field (i.e., no ferromagnetic materials can be present) are required. These challenges have now been overcome and the use of MR to study the product distribution of the ethene oligomerisation conversion occurring in a fixed-bed reactor operating at 110 °C and 28 barg has been reported (90). Second, the development and implementation of quantitative, spatially-resolved spectroscopy techniques are required that provide sufficient chemical discrimination that real chemical conversions can be studied over sufficiently short timescales for the reaction of interest. One approach to overcoming this challenge

is to use 2D NMR spectroscopy but reduce the intrinsically long data acquisition times by undersampling with compressed sensing reconstruction (91).

MR imaging of flow in reactors follows two main themes. First, direct observation of gas, liquid and solids distributions within the reactor and the velocity with which these phases are moving can give useful insight to reactor behaviour, even when the reaction itself is not occurring inside the magnet. Second, the level of temporal and spatial resolution that can now be achieved using MR techniques provides a level of detail that can discriminate between assumptions and theoretical models used in modelling hydrodynamics and reaction, as well as providing data that can be used to critically evaluate mathematical closures, selection of boundary conditions and direct validation of the predictions of numerical simulations.

Fixed Beds

High-resolution MRI investigations of fluid flow in fixed beds with column-to-particle diameter ratios that are typical of narrow fixed-bed reactors were first reported in the mid-1990s. Such measurements give insight to how flow within fixed beds should be modelled, as well as how particle sizes, shape and packing method influence hydrodynamics. Figure 1, shown earlier as a general example of MR velocity imaging in chemical engineering shows 2D sections through 3D volume images of the *x* and *z* components of flow within a fixed bed of non-porous spherical particles. The most striking characteristic of these images is the extent of heterogeneity in the flow field; a relatively small fraction of the inter-particle space carries a high percentage of the liquid flow (16,92,93). Such regions of the bed are associated with high fluid velocities, and inertial effects influence the flow profile (94). There are now numerous examples of MR being used in this application, sometimes alongside traditional reaction engineering characterisation such as residence time distribution analysis (95-98). In application to the benchmarking and validation of the predictions of flow simulators, MR is particularly valuable because it can provide data at high spatial resolution (20-300 μm, depending on the system) (99,100). Examples include the comparisons of MR flow images and propagators with the predictions of the same using a lattice-Boltzmann code (99). The advantage of using the lattice-Boltzmann simulation was that the MRI image of the packed bed is used directly as the 3D structure on which the numerical simulation is performed; there is no requirement for meshing. In comparing to the predictions of CFD codes (100), MR flow images also aid in the

selection of meshing algorithm and boundary conditions imposed in the implementation of the simulation.

Considering two-phase flow in fixed beds, gas-liquid distribution and velocity maps, the hydrodynamic transition from trickle to pulsing flow, and periodic operation of the bed have all been studied. Under conditions of trickle flow in which the spatial distribution of gas and liquid are constant, it has been shown that both holdup and wetting characteristics can be acquired (101), as can the gas and liquid velocity fields (102). A direct *in situ* measurement of solid wetting is particularly valuable since it cannot be obtained using any other technique and is often an explicit variable or included in a lumped parameter when modelling reactor behaviour. Whilst studies have focussed on co-current downflow, other modes of operation have been studied. In particular, gas phase dynamics has been studied during co-current up-flow. MR measurements of gas hold-up, bubble-size distribution, and bubble-rise velocities have been made as a function of gas and liquid flow rate and packing size (103). The gas hold-up was separated into a dynamic gas hold-up, only weakly dependent on packing size and associated with bubbles rising up the bed, and a 'static' hold-up associated with temporally-invariant gas hold-up associated either with gas trapped within the void structure of the bed or with gas channels within the bed.

MR has also been used to gain insight into reactor behaviour even if a reaction is not occurring within the bed on which the hydrodynamic measurements are made. For example, MR images have been acquired at a rate of 5 images per second so that the time evolution of liquid-solid (i.e. catalyst) contacting during periodic operation of a bed (104) can be studied. The MR images provide the bed characteristics in terms of the percentage of the bed associated with different liquid-solid contacting profiles which can then be used to model bed performance more accurately. These data were then used to show how different catalyst contacting profiles would influence catalyst effectiveness with reference to the hydrogenation of α-methylstyrene. More recently, MR has been used to image the gas-liquid distribution in a fixed bed as a function of temperature and suggest how these data may be used to gain greater understanding of the influence of hydrodynamics on desulfurization in bench-scale reactors (105).

MR has also been demonstrated to provide insights into the physical mechanism upon which the trickle-to-pulse transition in fixed beds should be based. As described by Larachi *et al.*

(106), there are two conceptually different approaches for describing the onset of the pulsing regime, these being the microscopic and macroscopic models. Microscopic models or single-pore models analyze pore-scale hydrodynamics and are based on the postulate that the macroscopic onset to pulsing flow is an outcome of a statistically large number of local pulsatile occurrences. In contrast, the macroscopic models are used to analyze the onset of pulsing at the reactor scale from a stability analysis of first-principle volume-averaged Navier-Stokes equations. Results determined by MR to characterize these phenomena suggest that the mechanism for this hydrodynamic transition is best described by local pulsatile events. The ultra-fast FLASH pulse sequence was used to acquire 3D images of liquid distribution within the bed as superficial liquid velocity was increased at constant gas superficial velocity (107,108). Each 3D image was acquired in 280 ms; in these images, signal intensity is associated only with the liquid phase. The variation in liquid content within each image pixel (voxel) over the complete time-series of images was then determined by calculating the standard deviation in pixel (voxel) intensity on a pixel-by-pixel basis. Regions characterized by low values of standard deviation identify stable gas-liquid distribution, whereas values of high standard deviation identify spatial locations in which the liquid content (gas-liquid distribution) is changing with time. Typical results of these experiments are shown in Figure 7. The data provided strong experimental evidence that isolated local pulsing events of order the size-scale of the packing elements are first formed. For constant gas flow rate, more local pulses are formed as liquid flow rate is increased. As liquid flow rate is increased further, the isolated local pulses join up until all the void space comprising the bed contains a time-varying liquid content. These data strongly supported the predictions of the theoretical model of the hydrodynamic transition proposed by Ng (109), thereby providing strong evidence that the origin of the hydrodynamic transition was the formation of liquid bridges across neighbouring packing elements, which then form isolated pulsing events which coalesce to create the fully pulsing state.

Gas-Solid Fluidised Beds

Using MR to study gas-solid fluidisation needs to be done in recognition of the limitations of MR in this application. First, imaging of the real solids used in a typical chemical engineering process is, in nearly all cases, not possible. This is because the nuclear spin relaxation times of the solid are usually so short that the resulting signal-to-noise of the resulting image is too low for a useful measurement. Ways of overcoming this are to study solids that contain a liquid-like centre; this might be a polymer shell filled with a liquid-like core (110), liquid saturate a

porous solid (111) (beware that it might dry during the data acquisition making the solid increasingly invisible to the MR experiment), or use a solid which has a naturally liquid-containing inner region. This is why seeds such as poppy seeds and mustard seeds are so widely used in studies of gas-solid fluidisation. All results discussed in this section use this approach. Second, the typical constraint on bed diameter being ~6 cm limits the ability of MR to study realistic column-scale hydrodynamics. It is important to recognise that it is not the MR experiment which cannot address larger column diameter but the diameter of commercially-available MR magnet hardware with large magnet bore diameters in a vertical configuration. However, as long as these limitations are acknowledged MR can, and has, contributed to our understanding of the fundamental aspects of gas-solid fluidisation. It is therefore important to design experiments in which column wall effects are minimised. Also, if MR is being used to aid the development of numerical codes of gas-solid hydrodynamics it is advisable to implement the simulation code such that it represents as closely as possible the environment in which the MR experiment is performed. Thus if wall effects are significantly present in the experiment, it is important to reflect that in the simulation.

Early works demonstrating the capability of MR to study various aspects of gas-solid fluidisation include the aforementioned work of Savelsberg *et al.* (111) who reported non-spatially resolved measurements of the solids flow field using fluidised beds of poppy seeds and acetone-filled catalyst particles to measure time-averaged density variations and also characterised the motion of the granular particles using pulsed field gradient measurements; the characterisation of mixing processes during fluidisation (112); and the distribution of solids just above a perforated plate distributor and imaging of the particle velocity field (113). Recently, imaging of the gas velocity field has been reported (114). Thus, analogous to the developments in fixed beds, it is now possible to image not only the distribution of gas and liquid but also the velocity fields of both. Again as with fixed beds SF_6 has been the gas imaged.

The introduction of fast MR techniques, as in the other fields discussed earlier in this review, opened up new opportunities in the study of gas-solid fluidisation. In particular, it became possible to track bubble and slug rise velocities. Most notably this was used by Müller *et al*. (115) who used a 1D imaging experiment to track bubble rise and slug velocities as well as the evolution of bubble size and velocity resulting from coalescence events. These MR experiments provided information on the dynamics of the granular flows with a temporal

resolution of ~1 ms, and were used in comparison with existing correlations for the prediction of bubble and slug rise velocities. Since then 2D and 3D imaging of solids distribution and associated velocity fields have been reported (116,117), with many studies focusing on jet shape and interactions between jets as a function of distributor design and gas flow rates (118-120). More challenging experiments have been reported which exploited the flexibility of MR to measure properties of particular relevance to a specific discipline. A good example of this is the use of MR to spatially-resolve measurements of granular temperature (121). In that work granular temperature provided an additional parameter with which to compare the prediction of Discrete Element Model (DEM) simulations; the dimensions of the bed in which the MR experiment was performed were replicated in the DEM simulation. The predictions of the DEM code were compared with the MR measurements of solids distribution, solids velocity and granular temperature as a function of the drag-force correlation used, as well as studying the effects of the value of coefficient of restitution and the thickness of the bed used in the simulation. Müller *et al.* (122) have summarised much of the work that has used MR to validate DEM simulation codes.

There has also been interest in comparing the data obtained from MR, ECT, X-ray and positron emission particle tracking methods to study gas-solid fluidisation (123-125). The take home message from these comparisons is not: 'which method is best?' Different tomographies and sensors are sensitive to different phenomena and are optimised for use at different sizescales of apparatus and at different spatial and temporal resolutions. Instead the value is in recognising the synergies between methods. There are also opportunities for measurements at high spatial resolution to aid in the image reconstruction algorithms used in intrinsically lower spatial resolution measurements; an example of this is when MR and Electrical Capacitance Volume Tomography (ECVT) are brought together to study the same system (123). In that work the two techniques were shown to provide quantitatively comparable time-averaged measurements of voidage and bubble frequencies.

CONCLUSIONS AND FUTURE OUTLOOK

Magnetic resonance is a highly flexible technique which has the great advantage of being able to probe both chemistry and transport. It is an intrinsically quantitative measurement, but the techniques have to be implemented with extreme care if that quantitative nature is to be

retained and the full value of the measurement achieved. In the context of chemical engineering the range of applications is now considerable. Areas of particular current interest, including those not covered in this review include:

- Use of images of gas-liquid distribution and species-specific diffusion, dispersion and flow for development and validation of theoretical models and numerical flow simulators.
- Increasing our ability to study multi-component catalytic processes within a reactor and discrimination of intra- and inter-(catalyst) pellet compositions. These measurements will not only test the design rules used in heterogeneous catalytic reactor design but will also directly aid catalyst development.
- Design of experiments which are directly relevant to industrial processes. This is not just about recreating the conditions of the industrial process but identifying the correct questions to be answered to aid the design and operation of the process.
- Increased use of undersampling methods in data acquisition and associated image reconstruction algorithms, alongside signal-enhancement techniques (126,127), to increase spatial and temporal resolution and our ability to track specific chemical species which may be present in low concentration.
- The translation of high magnetic field measurements to low cost, portable low magnetic field measurements which may be used as process sensors and for on-line analytics (128). This approach is well-established in the petrophysics area. So-called zero- to ultralow-field NMR (ZULF NMR) measurements (129) are in the very early stages of development and, in the longer term, might present opportunities for use as process sensors when high spectral resolution is required.

Magnetic resonance techniques and in particular MR imaging and velocity imaging can now be implemented with a level of robustness that they are making, and will continue to make, an increasing contribution to chemical engineering research.

REFERENCES

1. Callaghan PT. 1993. *Principles of Nuclear Magnetic Resonance Microscopy*. New York: Oxford University Press
2. Callaghan PT. 2011. *Translational Dynamics and Magnetic Resonance*. New York: Oxford University Press
3. Kleinberg RL, Kenyon WE, Mitra PP. 1994. Mechanism of NMR relaxation of fluids in rock. *J. Magn. Reson. A* 108:206-14
4. Godefroy S, Korb JP, Fleury M, Bryant RG. 2001. Surface nuclear magnetic relaxation and dynamics of water and oil in macroporous media. *Phys. Rev. E* 64:021605
5. Weber D, Mitchell J, McGregor J, Gladden LF. 2009. Comparing strengths of surface interactions for reactants and solvents in porous catalysts using two-dimensional NMR relaxation correlations. *J. Phys. Chem.* C 113:6610-15
6. Gladden LF, Mitchell J. 2011. Measuring adsorption, diffusion and flow in chemical engineering: applications of magnetic resonance to porous media. *New J. Phys.* 13:035001
7. Simoneau C, McCarthy MJ, Kauten RJ, German JB. 1991. Crystallization dynamics in model emulsions from magnetic resonance imaging. *J. Am. Oil. Chem. Soc.* 68:481-7
8. Mansfield P, Grannell PK. 1973. NMR diffraction in solids. *J. Phys. C.* 6:L422-6
9. Chen C, Gladden LF, Mantle MD. 2014. Direct visualization of *in vitro* drug mobilization from Lescol XL tablets using two-dimensional ^{19}F and ^{1}H magnetic resonance imaging. *Mol. Pharmaceutics* 11:630-7
10. Akpa BS, Mantle MD, Sederman AJ, Gladden LF. 2005. *In situ* ^{13}C DEPT-MRI as a tool to spatially resolve chemical conversion and selectivity of a heterogeneous catalytic reaction occurring in a fixed-bed reactor. *Chem. Commun.* 2741-3
11. Sederman AJ, Mantle MD, Dunckley CP, Huang Z, Gladden LF. 2005. *In situ* MRI study of 1-octene isomerisation and hydrogenation within a trickle-bed reactor. *Catal. Lett.* 103:1-8
12. Newling B, Poirier CC, Zhi Y, Rioux JA, Coristine AJ, Roach D, Balcom BJ. 2004. Velocity imaging of highly turbulent gas flow. *Phys. Rev. Lett.* 93:154503
13. Gladden LF. 2003. Magnetic resonance: Ongoing and future role in chemical engineering research. *AIChE J* 49:2-9

14. van de Meent J-W, Sederman AJ, Gladden LF, Goldstein RE. 2010. Measurement of cytoplasmic streaming in single cell plants by magnetic resonance velocimetry. *J. Fluid Mech.* 642:5-14
15. Sederman AJ, Mantle MD, Buckley C, Gladden LF. 2004. MRI technique for measurement of velocity vectors, acceleration, and autocorrelation functions in turbulent flow. *J. Magn. Reson.* 166:182-9
16. Sederman AJ and Gladden LF. 2001. Magnetic resonance visualization of single- and two-phase flow in porous media. *Magn. Reson. Imaging* 19:339-43
17. Singer PM, Leu G, Fordham EJ, Sen PN. 2006. Low magnetic fields for flow propagators in permeable rocks. *J. Magn. Reson.* 183:167-77
18. Scheven UM, Verganelakis, Harris R, Johns ML, Gladden LF. 2005. Quantitative nuclear magnetic resonance measurements of preasymptotic dispersion in flow through porous media. *Phys. Fluids* 17:117107
19. Johns ML, Sederman AJ, Gladden LF, Wilson A, Davies S. 2003. Using MR techniques to probe permeability reduction in rock cores. *AIChE J* 49:1076-84
20. Verganelakis DA, Crawshaw J, Johns ML, Mantle MD, Scheven U, Sederman AJ, Gladden LF. 2005. Displacement propagators of brine flowing within different types of sedimentary rock. *Magn. Reson. Imaging* 23:349-51
21. Edelstein WA, Hutchinson JMS, Johnson G, Redpath T. 1980. Spin warp NMR imaging and applications to human whole-body imaging. *Phys. Med. Biol.* 25:751-6
22. Hennig J, Nauerth A, Friedburg H. 1986. RARE imaging – a fast imaging method for clinical MRI. *Magn. Reson. Med.* 3:823-33
23. Mansfield P. 1977. Multi-planar image formation using NMR spin echoes. *J. Phys. C.* 10:L55-8
24. Haase A, Frahm J, Matthaei D, Hanicke W, Merboldt KD. 1986. FLASH imaging – rapid NMR imaging using low flip-angle pulses. *J. Magn. Reson.* 67:258-66
25. Mantle MD, Sederman AJ. 2003. Dynamic MRI in chemical process and reaction engineering. *Prog. Nucl. Mag. Res. Sp.* 43:3-60
26. Ahn CB, Kim JH, Cho ZH. 1986. High-speed spiral-scan echo planar NMR imaging. *IEEE Trans. Med. Imaging* 5:2-7
27. Tayler AB, Holland DJ, Sederman AJ, Gladden LF. 2011. Time resolved velocity measurements of unsteady systems using spiral imaging. *J. Magn. Reson.* 211:1-10
28. Nyquist H. 1928. Certain topics in telegraph transmission theory. *Trans. A.I.E.E.* 47:617-44
29. Shannon CE. 1949. Communication in the presence of noise. *Proc. I.R.E.* 37:10-21

30. Hogbom JA. 1974. Aperture synthesis with a non-regular distribution of interferometer baselines. *Astron. Astrophys. Suppl.* 15:417-26
31. Wiaux Y, Jacques L, Puy G, Scaife AMM, Vandergheynst P. 2009. Compressed sensing imaging techniques for radio interferometry. *Mon. Not. R. Astron. Soc.* 395:1733-42
32. Candès EJ, Romberg JK, Tao T. 2006. Stable signal recovery from incomplete and inaccurate measurements. *Commun. Pure Appl. Math.* 59:1207-23
33. Donoho DL. 2006. Compressed sensing. *IEEE Trans. Inf. Theory* 52:1289-1306
34. Lustig M, Donoho DL, Pauly JM. 2007. Sparse MRI: The application of compressed sensing for rapid MR imaging. *Mag. Reson. Med.* 58:1182-95
35. Bretthorst GL, Hung C, d'Avignon DA, Ackerman JJH. 1988. Bayesian analysis of time-domain magnetic resonance signals. *J. Magn. Reson.* 79:369-76
36. Bretthorst GL, Hutton WC, Garbow JR, Ackerman JJH. 2005. Exponential parameter estimation (in NMR) using Bayesian probability theory. *Concepts Magn. Reson. A* 27A:55-63
37. Xing D, Gibbs SJ, Derbyshire JA, Fordham EJ, Carpenter TA, Hall LD. 1995. Bayesian analysis for quantitative NMR flow and diffusion imaging. *J. Magn. Reson. B* 106:1-9
38. Wise RW, Newling B, Gates ARC, Xing D, Carpenter TA, Hall LD. 1996. Measurement of pulsatile flow using MRI and a Bayesian technique of probability analysis. *Magn. Reson. Imaging* 14:173-85
39. Benning M, Gladden L, Holland D, Schönlieb C-S, Valkonen T. 2014. Phase reconstruction from velocity-encoded MRI measurements – a survey of sparsity promoting variational approaches. *J. Magn. Reson.* 238:26-43
40. Holland DJ, Blake A, Tayler AB, Sederman AJ, Gladden LF. 2010. A Bayesian approach to characterising multi-phase flows using magnetic resonance: Application to bubble flow. *J. Magn. Reson.* 2011:83-7
41. Callaghan PT. 2008. Rheo NMR and shear banding. *Rheol. Acta* 47:243-55
42. Callaghan PT. 1999. Rheo-NMR: nuclear magnetic resonance and the rheology of complex fluids. *Rep. Prog. Phys.* 62:599-670
43. Hollingsworth KG, Johns ML. 2004. Rheo-nuclear magnetic resonance of emulsion systems. *J. Rheol.* 48:787-803
44. Domenico G, Migliori M, Di Sanzo R, Rossi CO, Ruffolo SA, de Cindio B. 2009. Characterisation of dairy emulsions by NMR and rheological techniques. *Food Hydrocolloid.* 23:619-28

45. Britton MM, Callaghan PT. 1997. Two-phase shear band structures at uniform stress. *Phys. Rev. Lett.* 78:4930-33
46. Britton MM, Callaghan PT. 1997. Nuclear magnetic resonance visualization of anomalous flow in a cone-and-plate geometry. *J. Rheol.* 41:1365-86
47. Douglass BS, Colby RH, Madsen LA, Callaghan PT. 2008. Rheo-NMR of wormlike micelles formed from nonionic pluronic surfactants. *Macromolecules* 41:804-14
48. Feindel KW, Callaghan PT. 2010. Anomalous shear banding: multidimensional dynamics under fluctuating slip conditions. *Rheol. Acta* 49:1003-13
49. Brown JR, Callaghan PT. 2011. Changing micellar order, lever rule behaviour and spatio-temporal dynamics in shear-banding at the onset of the stress plateau. *Soft Matter* 7:10472-82
50. Brown JR, Callaghan PT. 2010. Measurement of vorticity diffusion by NMR microscopy. *J. Magn. Reson.* 204:21-5
51. Davies CJ, Sederman AJ, Pipe CJ, McKinley GH, Gladden LF, Johns ML. 2010. Rapid measurement of transient velocity evolution using GERVAIS. *J. Magn. Reson.* 202:93-101
52. Evertz LQ, Rassi EM, Kennedy JRM, Codd SL, Seymour JD. 2012. Oscillatory flow phenomena in simple and complex fluids. *Appl. Magn. Reson.* 42:211-25
53. Blythe TW, Sederman AJ, Mitchell J, Stitt EH, York APE, Gladden LF. 2015. Characterising the rheology of non-Newtonian fluids using PFG-NMR and cumulant analysis. *J. Magn. Reson.* 255:122-131
54. Packer KJ, Rees C. 1972. Pulsed NMR studies of restricted diffusion. I. Droplet size distributions in emulsions. J. Colloid Interf. Sci. 40:206-18
55. Johns ML, Hollingsworth. 2007. Characterisation of emulsion systems using NMR and MRI. *Prog. Nucl. Mag. Res. Sp.* 50:51-70
56. Lingwood IA, Chandrasekera TC, Kolz J, Fridjonsson EO, Johns ML. 2012. Emulsion droplet sizing using low-field NMR with chemical shift resolution and the block gradient pulse method. *J. Magn. Reson.* 214:281-88
57. Hafid H, Ovarlez G, Toussaint F, Jezequel PH, Roussel N. 2015. Assessment of potential concrete and mortar rheometry artifacts using magnetic resonance imaging. *Cement Concrete Res.* 71:29-35
58. Fall A, Bertrand F, Hautemayou D, Mezière C, Moucheront P, Lemaître, Ovarlez G. 2015. Macroscopic discontinuous shear thickening versus local shear jamming in cornstarch. *Phys. Rev. Lett.* 114:098301

59. de Cagny H, Fall A, Denn MM, Bonn D. 2015. Local rheology of suspensions and dry granular materials. *J. Rheol.* 59:957-69
60. Oh S, Song Y-Q, Garagash DI, Lecampion B, Desroches J. 2015. Pressure-driven suspension flow near jamming. *Phys. Rev. Lett.* 114:088301
61. Harich R, Blythe TW, Hermes M, Zaccarelli E, Sederman AJ, Gladden LF, Poon WCK. 2016. Gravitational collapse of depletion-induced colloidal gels. *Soft Matter* 12:4300-8
62. Akpa BS, Matthews SM, Sederman AJ, Yunus K, Fisher AC, Johns ML, Gladden LF. 2007. Study of miscible and immiscible flows in a microchannel using magnetic resonance imaging. *Anal. Chem.* 79:6128-34
63. Zhang J, Balcom BJ. 2010. Magnetic resonance imaging of two-component liquid-liquid flow in a circular capillary tube. *Phys. Rev. E* 81:056318
64. Xia Y, Callaghan PT, Jeffrey KR. 1992. Imaging velocity profiles: Flow through an abrupt contraction and expansion. *AIChE J* 38:1408-20
65. Mullin T, Seddon JRT, Mantle MD, Sederman AJ. 2009. Bifurcation phenomena in the flow through a sudden expansion in a circular pipe. *Phys. Fluids* 21:014110
66. Jossic L, Magnin A. 2005. Structuring of gelled suspensions flowing through a sudden three-dimensional expansion. *J. Non-Newton. Fluid.* 127:201-12
67. Moraczewski T, Shapley NC. 2006. The effect of inlet conditions on concentrated suspension flows in abrupt expansions. *Phys. Fluids* 18:123303
68. Tozzi EJ, Lavenson DM, McCarthy MJ, Powell RL. 2013. Effect of fiber length, flow rate, and concentration on velocity profiles of cellulosic fiber suspensions. *Acta. Mech.* 224:2301-10
69. Singer JR. 1959. Blood flow rates by nuclear magnetic resonance measurements. *Science* 130:1652-3
70. Osán TM, Ollé JM, Carpinella M, Cerioni LMC, Pusiol DJ, Appel M, Freeman J, Espejo I. 2011. Fast measurements of average flow velocity by low-field ^{1}H NMR. *J. Magn. Reson*. 209:116-22
71. Fridjonsson EO, Stanwix PL, Johns ML. 2014. Earth's field NMR flow meter: Preliminary quantitative measurements. *J. Magn. Reson.* 245:110-5
72. Tayler AB, Holland DJ, Sederman AJ, Gladden LF. 2012. Applications of ultra-fast MRI to high voidage bubbly flow: Measurement of bubble size distributions, interfacial area and hydrodynamics. *Chem. Eng. Sci.* 71:468-83
73. Holland DJ, Blake A, Tayler AB, Sederman AJ, Gladden LF. 2012. Bubble size measurement using Bayesian magnetic resonance. *Chem. Eng. Sci.* 84:735-45

74. Tayler AB, Holland DJ, Sederman AJ, Gladden LF. 2012. Exploring the origins of turbulence in multiphase flow using compressed sensing MRI. *Phys. Rev. Lett.* 108:264505
75. Mougin G, Magnaudet J. 2002. Path instability of a rising bubble. *Phys. Rev. Lett.* 88:014502
76. Shew WL, Pinton J.-F. 2006. Dynamical model of bubble path instability. *Phys. Rev. Lett.* 97:144508
77. Gladden LF, Mantle MD, Sederman. 2005. Quantifying physics and chemistry at multiple length-scales using magnetic resonance techniques. *Adv. Chem. Eng.* 30:63-135
78. Gladden LF, Mantle MD, Sederman. 2006. Magnetic resonance imaging of catalysts and catalytic processes. *Adv. Catal.* 50:1-75
79. Koptyug IV, Ilyina LY, Matveev AV, Sagdeev RZ, Parmon VN, Altobelli SA. 2001. Liquid and gas flow and related phenomena in monolithic catalysts studied by ^{1}H NMR micrimaging. *Catal. Today* 69:385-92
80. Heibel AK, Scheenen TWJ, Heiszwolf JJ, van As H, Kapteijn F, Moulijn JA. 2001. Gas and liquid phase distribution and their effect on reactor performance in the monolith film flow reactor. *Chem. Eng. Sci.* 56:5935-44
81. Mantle MD, Sederman AJ, Gladden LF, Raymahasay S, Winterbottom JM, Stitt EH. 2002. Dynamic MRI visualization of two-phase flow in a ceramic monolith. *AIChE J* 48:909-12.
82. Heibel AK, Vergeldt FJ, van AS H, Kapteijn F, Moulijn J, Boger T. 2003. Gas and lquid distribution in the monolith film flow reactor. *AIChE J* 49:3007-17
83. Sederman AJ, Heras JJ, Mantle MD, Gladden LF. 2007. MRI strategies for characterising two-phase flow in parallel channel ceramic monoliths. *Catal. Today* 128:3-12
84. Ramskill NP, Gladden LF, York APE, Sederman AJ, Mitchell J, Hardstone KA. 2013. Understanding the operation and preparation of diesel particulate filters using a multi-faceted nuclear magnet resonance approach. *Catal. Today* 216:104-110
85. Yuen EHL, Sederman AJ, Gladden LF. 2002. *In situ* magnetic resonance visualisation of the spatial variation of catalytic conversion within a fixed-bed reactor. *Appl. Catal. A* 232:29-38
86. Koptyug IV, Lysova, Kulikov AV, Kirillov, Parmon VN, Sagdeev RZ. 2004. Functional imaging and NMR spectroscopy of an operating gas-liquid-solid catalytic reactor. *Appl. Catal. A* 267:143-8

87. Kirillov VA, Koptyug IV. 2005. Critical phenomena in trickle-bed reactors. *Ind. Eng. Chem. Res.* 44:9727-38
88. Gladden LF, Abegão FJR, Dunckley CP, Holland DJ, Sankey MH, Sederman AJ. MRI: *Operando* measurements of temperature, hydrodynamics and local reaction rate in a heterogeneous catalytic reactor. 2010. *Catal. Today* 155:157-63
89. Ulpts J, Dreher W, Klink M, Thöming J. 2015. NMR imaging of gas phase hydrogenation in a packed bed flow reactor. *Appl. Catal. A* 502:340-9
90. Roberts ST, Renshaw MP, Lutecki M, McGregor J, Sederman AJ, Mantle MD, Gladden LF. 2013. *Operando* magnetic resonance: monitoring the evolution of conversion and product distribution during the heterogeneous catalytic ethane oligomerisation reaction. *Chem. Commun*. 49: 10519-21
91. Wu Y, d'Agostino C, Holland DJ, Gladden LF. 2014. *In situ* study of reaction kinetics using compressed sensing NMR. *Chem. Commun*. 50:14137-40
92. Sederman, AJ, Johns ML, Bramley AS, Alexander P, Gladden LF. 1997. Magnetic resonance imaging of liquid flow and pore structure within packed beds. *Chem. Eng. Sci.* 52:2239-50
93. Sederman AJ, Johns ML, Alexander P, Gladden LF. 1998. Structure-flow correlations in packed beds. *Chem. Eng. Sci.* 53:2117-28
94. Johns ML, Sederman AJ, Bramley AS, Gladden LF, Alexander P. 2000. Local transitions in flow phenomena through packed beds identified by MRI. *AIChE J* 46:2151-61
95. Manz B, Alexander P, Gladden LF. 1999. Correlations between dispersion and structure in porous media probed by nuclear magnetic resonance. *Phys. Fluids* 11:259-67.
96. Götz J, Zick K, Heinen C, König T. 2002. Visualisation of flow processes in packed beds with NMR imaging: determination of the local porosity, velocity vector and local dispersion coefficients. *Chem. Eng. Process.* 41:611-29
97. Suekane T, Yokouchi Y, Hirai S. 2003. Inertial flow structures in a single-packed bed of spheres. *AIChE J* 49:10-17
98. Tang D, Jess A, Ren X, Blümich B, Stapf S. 2004. Axial dispersion and wall effects in narrow fixed bed reactors: A comparative study based on RTD and NMR measurements. *Chem. Eng. Technol*. 27:866-73
99. Manz B, Gladden LF, Warren PB. 1999. Flow and dispersion in porous media: Lattice-Boltzmann and NMR studies. *AIChE J* 45:1845-54
100. Robbins DJ, El-Bachir MS, Gladden LF, Cant RS, von Harbou E. 2012. CFD modelling of single-phase flow in a packed bed with MRI validation. *AIChE J* 58:3904-15

101. Sederman AJ, Gladden LF. 2001. Magnetic resonance imaging as a quantitative probe of gas-liquid distribution and wetting efficiency in trickle-bed reactors. *Chem. Eng. Sci.* 2001:2615-28
102. Sankey MH, Holland DJ, Sederman AJ, Gladden LF. 2009. Magnetic resonance velocity imaging of liquid and gas two-phase flow in packed beds. *J. Magn. Reson.* 196:142-8
103. Gladden LF, Collins J, Sederman A, Afeworki M, Kushnerick JD, Thomann H. 2016. Characterising gas behaviour during gas-liquid co-current up-flow in packed beds using magnetic resonance imaging. *Chem. Eng. Sci.* In press
104. Dietrich W, Anadon L, Sederman A, Gladden L, Agar D. 2012. Simulation studies on the performance enhancement in periodically operated trickle-bed reactors based on experimental local liquid distribution measurements. *Ind. Eng. Chem. Res.* 51:1672-9
105. Nguyen NL, Reimert R, Hardy EH. 2006. Application of magnetic resonance imaging (MRI) to determine the influence of fluid dynamics on desulfurization in bench scale reactors. *Chem. Eng. Technol.* 29:820-7
106. Larachi F, Iliuta I, Chen M, Grandjean BPA. 1999. Onset of pulsing in trickle beds: Evaluation of current tools and state-of-the-art correlation. *Can. J. Chem. Eng.* 77:751-8
107. Gladden LF, Anadon LD, Lim MHM, Sederman AJ, Stitt EH. 2005. Insights into the mechanism of the trickle-to-pulse transition in trickle-bed reactors. *Ind. Eng. Chem. Res.* 44:6320-31
108. Anadon LD, Sederman AJ, Gladden LF. 2006. Mechanism of the trickle-to-pulse transition in fixed-bed reactors. *AIChE J* 52:1522-32
109. Ng KM. 1986. A model for het flow regime transitions in concurrent downflow trickle-bed reactors. *AIChE J* 32:114-22
110. Lasič S, Stepišnik J, Mohorič A, Serša I, Planinšič. 2006. Autocorrelation spectra of an air-fluidized granular system measured by NMR. *Europhys. Lett.* 75:887-93
111. Savelsberg R, Demco DE, Blümich B, Stapf S. 2002. Particle motion in gas-fluidized granular systems by pulsed-field gradient nuclear magnetic resonance. *Phys. Rev. E* 65:020301
112. Fennell PS, Davidson JF, Dennis JS, Gladden LF, Hayhurst AN, Mantle MD, Müller CR, Rees AC, Scott SA, Sederman AJ. 2005. A study of the mixing of solids in gas-fluidized beds, using ultra-fast MRI. *Chem. Eng. Sci.* 60:2085-88
113. Rees AC, Davidson JF, Dennis JS, Fennell PS, Gladden LF, Hayhurst AN, Mantle MD, Müller CR, Sederman AJ. 2006. The nature of the flow just above the perforated plate

distributor of a gas-fluidised bed, as imaged using magnetic resonance. *Chem. Eng. Sci.* 61:6002-15

114. Boyce CM, Rice NP, Davidson JF, Sederman AJ, Dennis JS, Holland DJ. 2016. Magnetic resonance imaging of gas dynamics in the freeboard of fixed beds and bubbling fluidized beds. *Chem. Eng. Sci.* 147:13-20
115. Müller CR, Davidson JF, Dennis JS, Fennell PS, Gladden LF, Hayhurst AN, Mantle MD, Rees AC, Sederman AJ. 2006. Real-time measurement of bubbling phenomena in a three-dimensional gas-fluidized bed using ultrafast magnetic resonance imaging. *Phys. Rev. Lett.* 96:154504
116. Müller CR, Holland DJ, Davidson JF, Dennis JS, Gladden LF, Hayhurst AN, Mantle MD, Sederman AJ. 2007. Rapid two-dimensional imaging of bubbles and slugs in a three-dimensional, gas-solid, two-phase flow system using ultrafast magnetic resonance. *Phys. Rev. E* 75:020302
117. Müller CR, Holland DJ, Sederman AJ, Dennis JS, Gladden LF. 2010. Magnetic resonance measurements of high-velocity particle motion in a three-dimensional gas-solid spouted bed. *Phys. Rev. E* 82:050302
118. Pore M, Holland DJ, Chandrasekera TC, Müller CR, Sederman AJ, Dennis JS, Gladden LF, Davidson JF. 2010. Magnetic resonance studies of a gas-solids fluidised bed: Jet-jet and jet-wall interactions. *Particuology* 8:617-22
119. Pore M, Chandrasekera TC, Holland DJ, Wang A, Wang F, Marashdeh Q, Mantle MD, Sederman AJ, Fan L-S, Gladden LF. 2012. Magnetic resonance studies of jets in a gas-solid fluidised bed. *Particuology* 10:161-9
120. Köhl MH, Lu G, Third JR, Häberlin M, Kasper L, Prüssmann KP, Müller CR. 2013. Magnetic resonance imaging (MRI) study of jet formation in packed beds. *Chem. Eng. Sci.* 97:406-12
121. Müller CR, Holland DJ, Sederman AJ, Scott SA, Dennis JS, Gladden LF. 2008. Granular temperature: Comparison of magnetic resonance measurements with Discrete Element Model simulations. *Powder Technol.* 184:241-53
122. Müller CR, Holland DJ, Third JR, Sederman AJ, Dennis JS, Gladden LF. 2011. Multi-scale magnetic resonance measurements and validation of Discrete Element Model simulations. *Particuology* 9:330-41
123. Holland DJ, Mareshdeh Q, Müller CR, Wang F, Dennis JS, Fan L-S, Gladden LF. 2009. Comparison of ECVT and MR measurements of voidage in a gas-fluidized bed. *Ind. Eng. Chem. Res.* 48:172-81

124. Chandrasekera TC, Wang A, Holland DJ, Mareshdeh Q, Pore M, Wang F, Sederman AJ, Fan L-S, Gladden LF, Dennis JS. 2012. A comparison of magnetic resonance imaging and electrical capacitance tomography: An air jet through a bed of particles. *Powder Technol.* 227:86-95
125. Pore M, Ong GH, Boyce CM, Materazzi M, Gargiuli, Leadbetter T, Sederman AJ, Dennis JS, Holland DJ, Ingram A, Lettieri P, Parker DJ. 2015. A comparison of magnetic resonance, X-ray and positron emission particle tracking measurements of a single jet of gas entering a bed of particles. *Chem. Eng. Sci.* 122:210-8
126. Glöggler S, Colell J, Appelt S. 2013. Para-hydrogen perspectives in hyperpolarized NMR. *J. Magn. Reson.* 235:130-42
127. Graafen D. 2014. ^{1}H NMR spectroscopy and MR imaging with hyperpolarised substances. *Ann. R. NMR S.* 82:167-215
128. Mitchell J, Gladden LF, Chandrasekera TC, Fordham EJ. 2014. Low-field permanent magnets for industrial process and quality control. *Prog. Nucl. Mag. Res. Sp.* 76:1-60
129. Blanchard JW, Sjolander TF, King JP, Ledbetter MP, Levine EH, Bajaj VS, Budker D, Pines A. 2015. Measurement of untruncated nuclear spins interactions via zero- to ultralow-field nuclear magnetic resonance. *Phys. Rev. B* 92:220202

Figure Captions

Figure 1

MR visualisation of water flowing within a fixed bed of spherical glass beads (16); the beads have no MR signal intensity associated with them and are identified as black voxels. Flow velocities in the (a) z- and (b) x-directions are shown with slices taken in the xy, yz and xz planes for each of the velocity components; z is the direction of superficial flow. For each image the positions at which the slices in the other two directions have been taken are identified. Isotropic voxel resolution is 195 μm. The glass beads are of diameter 5 mm and are packed within a column of internal diameter 46 mm.

Figure 2

Example of MR propagators as used to characterise molecular transport in porous rock core plugs: (a) Bentheimer sandstone, and (b) Portland carbonate. Here the data are shown normalised to the nominal mean displacement for the particular observation time, Δ. In this example, Δ ranges from 106-2000 ms. The Portland core exhibits a larger stagnant population than is observed for the Bentheimer core, along with flow in a relatively high velocity channel consistent with the differences in pores structure shown by the scanning electron microscopy images. The width of the images shown corresponds to 3.0 mm and 7.1 mm for the Bentheimer and Portland samples, respectively (18,20).

Figure 3

Different **k**-space sampling patterns. The **k**-space rasters are shown by the green dots in each case. a) Rectilinear sampling of every line in **k**-space typical of spin warp imaging; b) a spiral sampling pattern; c) undersampling of the spin warp imaging scheme in a) as would be typically used for compressed sensing reconstruction and; d) where a Bayesian model is employed, a very small sub-section of **k**-space may be acquired. d) shows a sampling pattern that might be used to extract information about a particular length-scale, L, of interest in the sample where $k' = \frac{1}{L} = \frac{\gamma G t}{2\pi}$.

Figure 4

Velocity images (a, c) and shear-rate maps (b,d) for a wormlike surfactant solution in a 4˚ cone and plate rheometer acquired at shear rates of 1.5 s^{-1} (a,b) and 16 s^{-1} (c,d). The vertical axis in these images has been expanded so that the flow field can be seen more easily. The colour scale represents velocities and shear rates ranging between ±0.9 mm s^{-1} and ±0.05 s^{-1}, respectively (a,b); and ±12 mm s^{-1} and ±57 s^{-1}, respectively (c,d). Adapted from (46).

Figure 5

Measuring different information about flow downstream of an abrupt expansion (65). a) velocity image at Re = 946; b) a RARE intensity image at the same Re as in a). Signal intensity in the RARE image identifies zero flow regions at the wall and in a bright ring between the backflow region close to the walls and the forward flowing jet. c) A RARE intensity image at Re = 1567 showing the asymmetry of the jet that develops as Re increases. Data are recorded 36 cm downstream of the expansion.

Figure 6

Velocity maps about a single bubble rising freely through stagnant solution. The location of the bubble is identified by the filled white ellipses. The acquisition rate was 63 fps. The spatial resolution is 390 μm × 586 μm for a field of view of 20 mm × 30 mm. Adapted from (74).

Figure 7

Imaging the evolution of the trickle-to-pulse transition in a fixed bed of porous cylindrical alumina pellets of height and length 3 mm (108). 3D standard deviation maps of a vertical section of height 4 cm. The bed is operating at a constant gas velocity of 300 mm s^{-1}, at liquid velocities a) 3.9, b) 6.1, c) 8.1 and d) 12.2 mm s^{-1}. Red on the colour bar indicates a high value of standard deviation and therefore identifies unstable liquid content as a function of time. Under conditions of trickle flow (a), the liquid distribution within the bed is stable. The highlighted regions in (b) identify local pulsing regions.

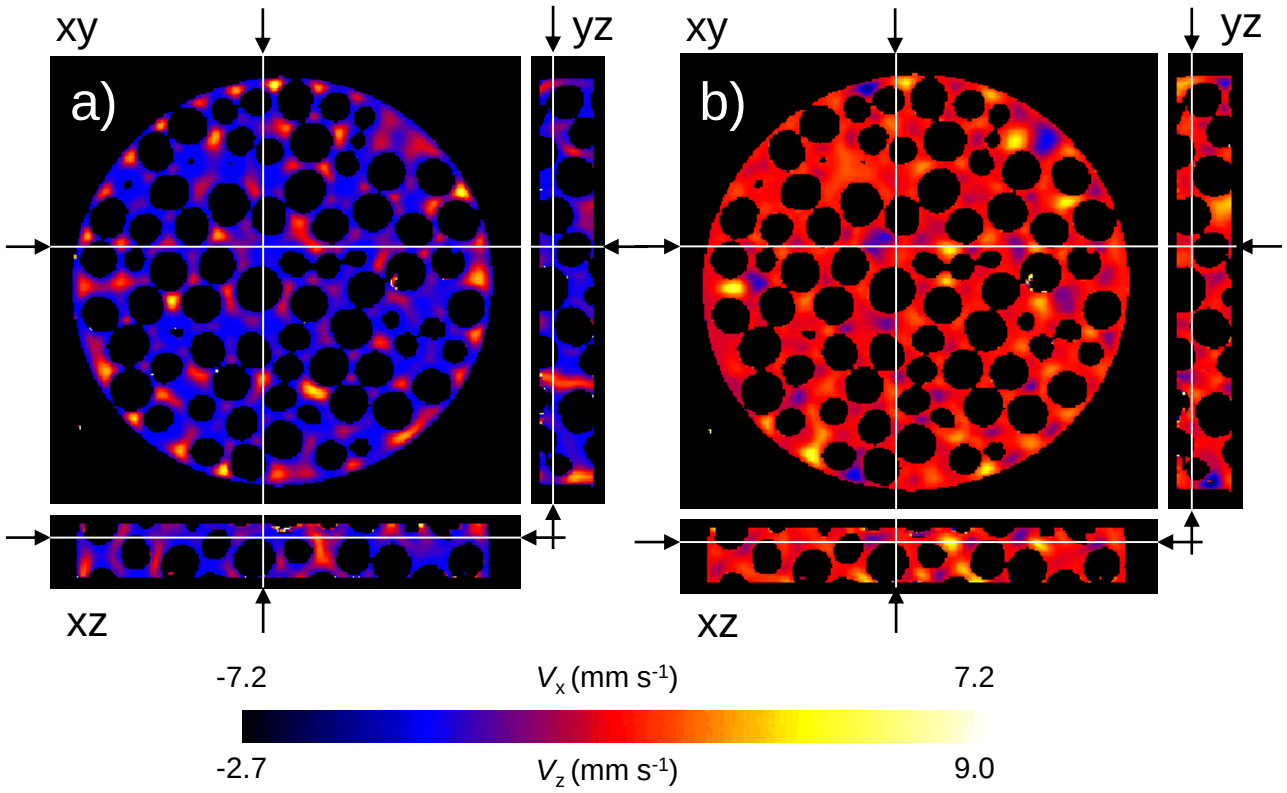

Figure 1

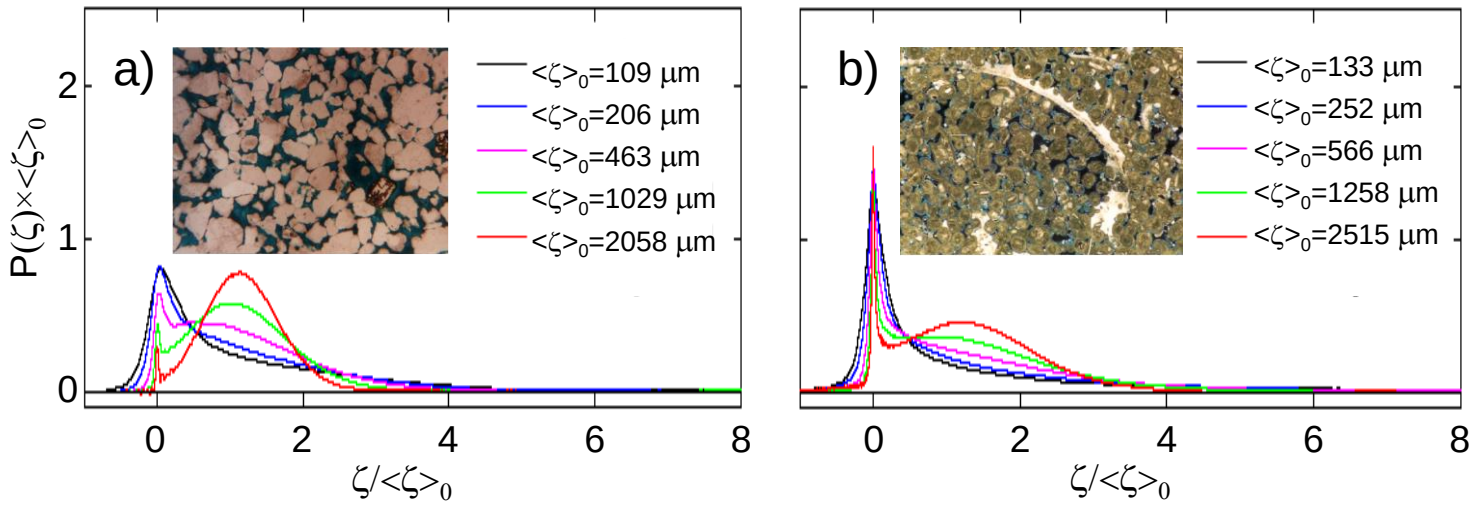
a)
b)
P(ζ)×<ζ>0
ζ/<ζ>0
<ζ>0=109 µm
<ζ>0=206 µm
<ζ>0=463 µm
<ζ>0=1029 µm
<ζ>0=2058 µm
<ζ>0=133 µm
<ζ>0=252 µm
<ζ>0=566 µm
<ζ>0=1258 µm
<ζ>0=2515 µm

Figure 2

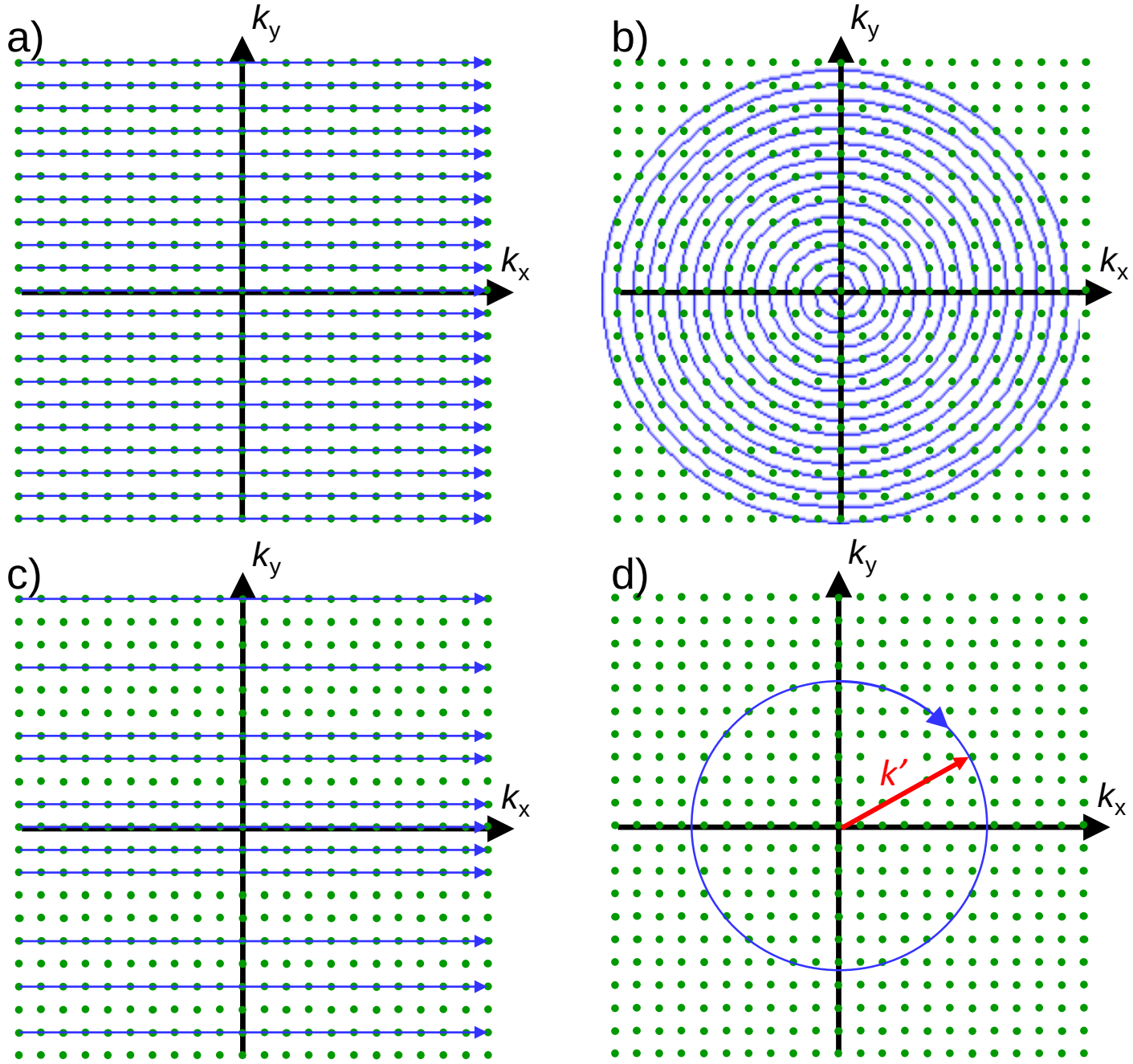

Figure 3

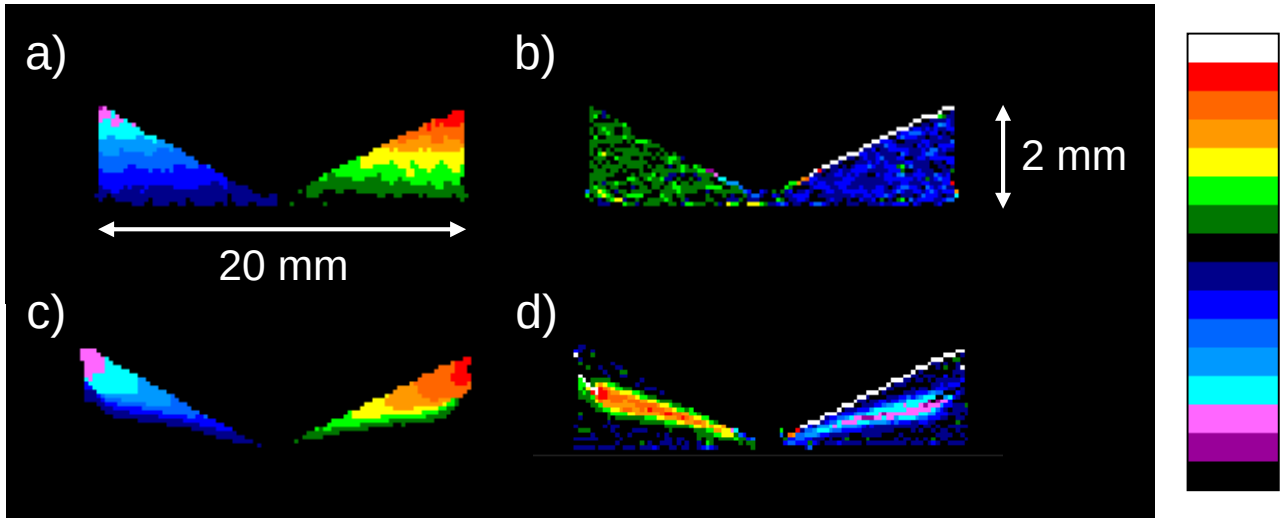

Figure 4

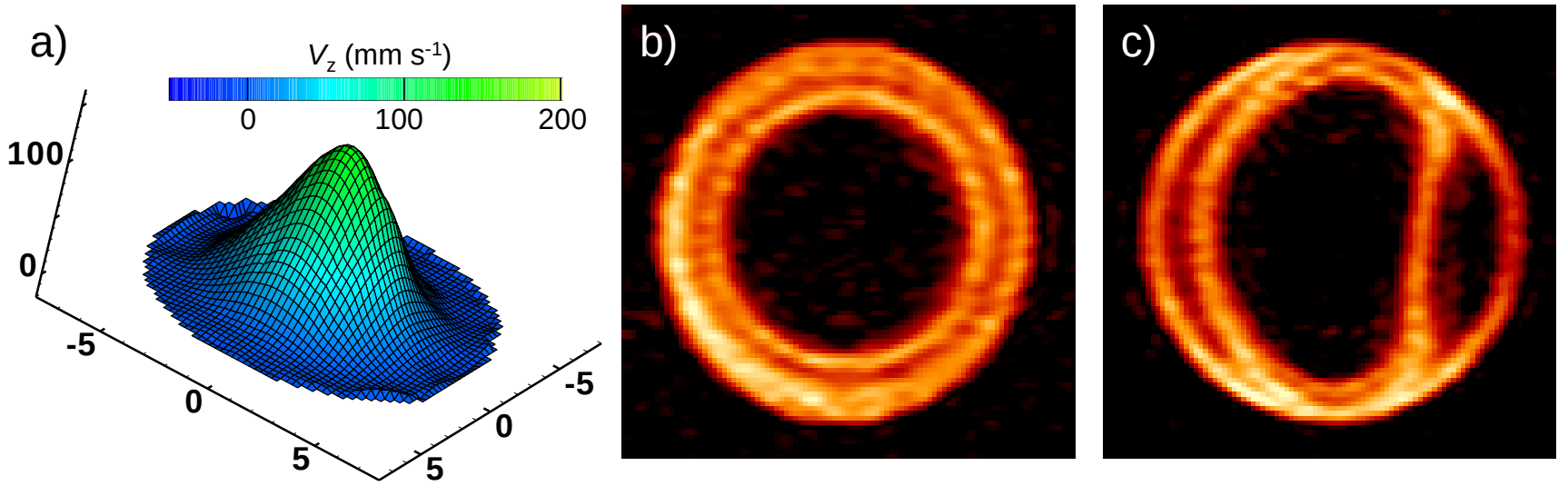

Figure 5

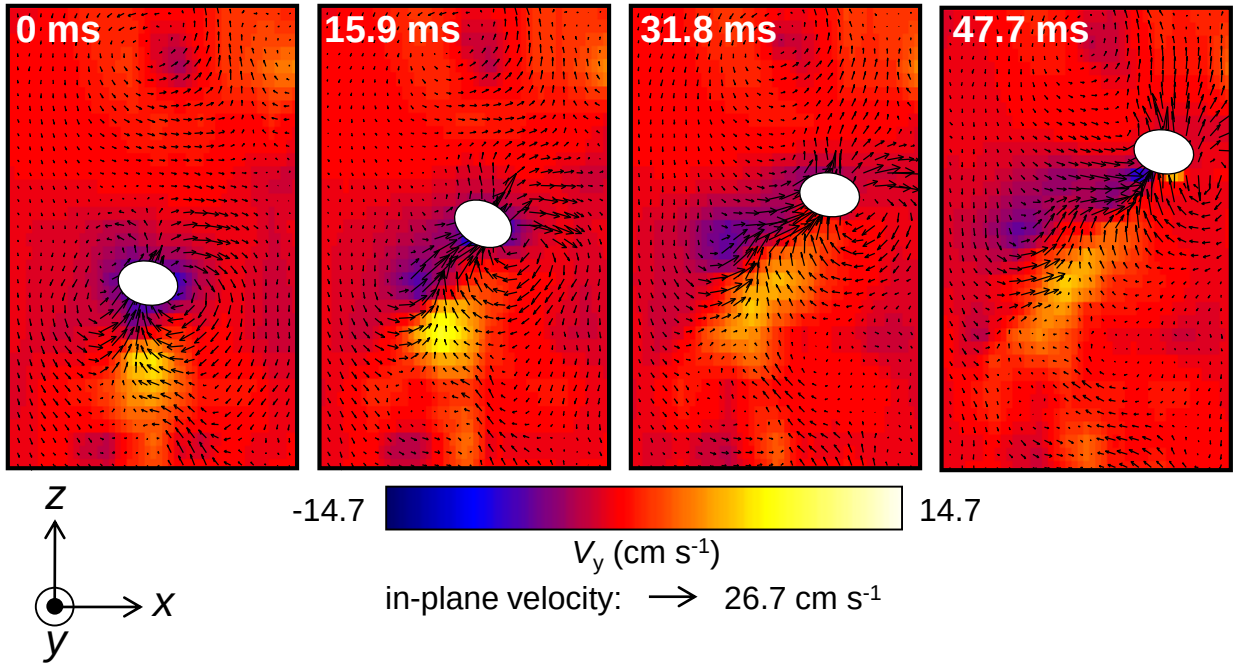
0 ms
15.9 ms
31.8 ms
47.7 ms
z
x
y
-14.7
14.7
V_y (cm s^{-1})
in-plane velocity: → 26.7 cm s^{-1}

Figure 6

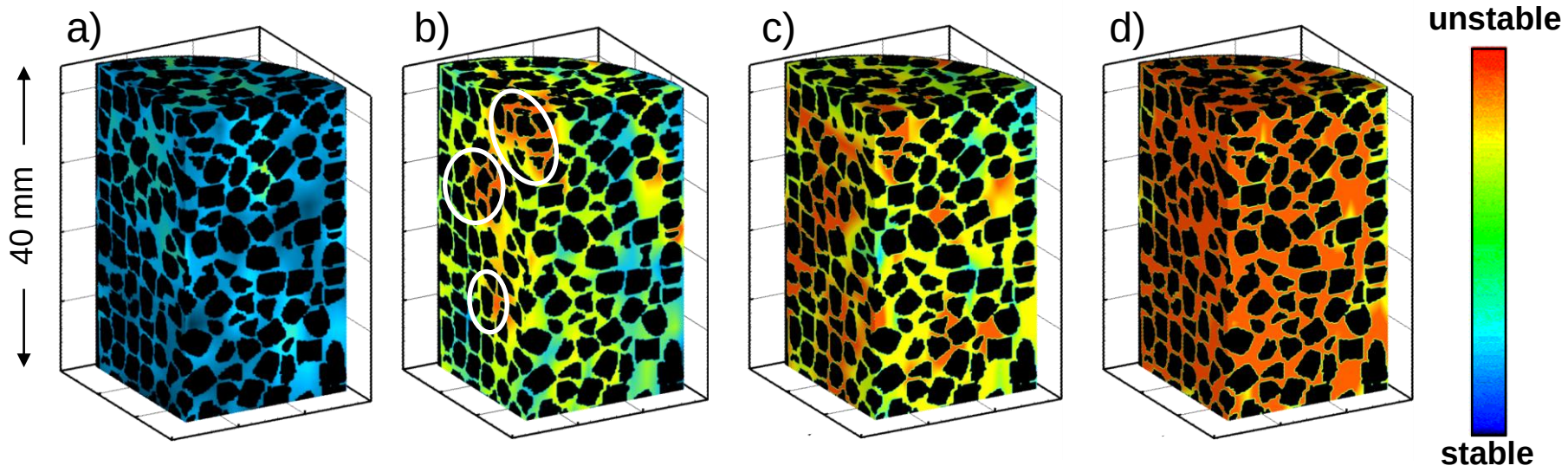

Figure 7